Int J Appl Earth Obs Geoinformation 87 (2020) 102050

Contents lists available at ScienceDirect

Int J Appl Earth Obs Geoinformation

journal homepage: www.elsevier.com/locate/jag

Investigation of the ground displacement in Saint Petersburg, Russia, using multiple-track differential synthetic aperture radar interferometry

Qiang Wang[a,b,c], Qing Zhao[a,b,c,*], Jingzhao Ding[a,b,c], Alexander A. Fedotov[d], Vladimir Badenko[d], Min Liu[a,b,c], Antonio Pepe[e]

[a] Key Laboratory of Geographical Information Science, Ministry of Education, East China Normal University, Shanghai, 200062, China
[b] Institute of Eco-Chongming (IEC), East China Normal University, Shanghai, 202162, China
[c] School of Geographic Sciences, East China Normal University, Shanghai, 200241, China
[d] Peter the Great St. Petersburg Polytechnic University, Civil Engineering Institute, 195251 Polytechnicheskaya 29, Russia
[e] Institute for Electromagnetic Sensing of the Environment (IREA), Italian National Research Council, 328 Diocleziano, Napoli, 80124, Italy

ARTICLE INFO

Keywords:
Ground displacements
Synthetic aperture radar interferometry
Flooding

ABSTRACT

Global sea level rise and local land subsidence might exacerbate the risk of flooding in coastal plains. Among other cities, this is also the case for the high-latitude city of St. Petersburg, which has long been threatened by flood events. To protect the urban area from storm surges, the Union of Soviet Socialist Republics (USSR) in 1978 approved the construction of the 25 km long Flood Prevention Facility Complex (FPFC), which was completed in 2011. The risk of flooding in the city area of St. Petersburg is amplified by the fact that large sections of the coastal area have been reclaimed from the sea. In this study, we investigate the temporal evolution of the ground displacement in St. Petersburg. To this end, we perform an extended analysis based on the application of a simplified version of the differential interferometric synthetic aperture radar technique, known as the minimum acceleration (MinA) approach. The MinA algorithm is a multi-satellite/multi-track interferometric combination technique that allows working with multiple sets of SAR images. The method allowed generation of time series of two-dimensional (2-D) (i.e. East-West and Up-Down) deformation of the terrain by processing two sequences of Sentinel-1A/B (S-1A/B) SAR images acquired from 2016 to 2018, along the ascending and descending flight passes. The Small BAseline Subset (SBAS) algorithm was independently applied to the two sets of SAR data to generate the relevant Line-Of-Sight (LOS)-projected ground deformation time series. Subsequently, the LOS-projected deformation products were geocoded and jointly combined. The results indicate that the deformation in the city is predominantly vertical (i.e. it is subsiding) with a maximum subsidence rate of about 20 mm/year corresponding to the newly sea-reclaimed lands. Finally, the error budget of the retrieved 2-D deformation time series has also been addressed.

1. Introduction

Coastal areas are rapidly becoming the most densely populated regions in the world, owing to the convenient transportation facilities, the pleasant ecological environments, and the developed economies. However, many of the coastal cities are subjected to severe natural and anthropogenically induced disasters, such as, flooding, storm surges, and land subsidence (Colle et al., 2008; Wang et al., 2012). Continuous land subsidence in coastal cities not only leads to remarkable economic losses owing to the high costs of maintenance, but also increases the risk of flooding (Yin et al., 2016). Thus, it is crucial to monitor the temporal evolution of the ground deformation regularly, with a particular eye on the stability of the flood protection facilities. The present work is focused on the study of the ground deformations in St. Petersburg, Russia. Only a few studies characterising the ground deformation status of the city have been published in recent years (Dashko and Lebedeva, 2017; Filippova and Matyushina, 2016; Kozin, 2016; Novozhenin and Vystrchil, 2016; Ulitsky et al., 2005).

Consequently, the recent distribution pattern of ground deformation in the city is still not well constrained. Our investigation relies on the application of the differential interferometric synthetic aperture radar technology (Massonnet and Feigl, 1998) that plays a critical role in detecting and monitoring the surface ground deformations of the Earth. For the past two decades, the development of advanced multi-temporal interferometric synthetic aperture radar (InSAR) techniques (e.g., Berardino et al., 2002; Ferretti et al., 2001; Hooper et al., 2004), has

* Corresponding author at: Key Laboratory of Geographical Information Science, Ministry of Education, East China Normal University, Shanghai, 200062, China.
E-mail address: qzhao@geo.ecnu.edu.cn (Q. Zhao).

https://doi.org/10.1016/j.jag.2020.102050
Received 24 April 2019; Received in revised form 11 December 2019; Accepted 6 January 2020
Available online 11 January 2020

allowed large-scale monitoring of the changes in the surface of the Earth by generating time series of terrain deformation using sequences of SAR images collected at different times. The multi-temporal InSAR (MT-InSAR) techniques have already been successfully applied to study the deformations in coastal mega-cities (e.g., Aimaiti et al., 2018; Xu et al., 2016). However, conventional MT-InSAR techniques can only compute the projection of the surface deformation along the radar Line-of-Sight (LOS) direction and are unable to provide suitable information on the three-dimensional (3-D) shape of the ground terrain displacement. The growing availability of SAR images collected at complementary viewing angles by constellations of SAR satellites has recently made it possible to distinguish and compute the 3-D components of the surface deformation (East-West, Up-Down, North-South) (Gray, 2011; Tofani et al., 2013; Pepe et al., 2016; Wright et al., 2004). In particular, the approach known as minimum acceleration (MinA) combination technique (Pepe et al., 2016) represents a suitable post-processing InSAR tool that allows the generation of time series of 3-D deformation (and associated mean deformation velocity maps) with increased measurements temporal samplings. In our study, a simplified version of the MinA technique that computes time series of two-dimensional (2-D; Up-Down and East-West) ground deformations has been applied to study the ground deformations in St. Petersburg. In particular, the relationship between the on-going ground terrain displacement in the coastal city and its exposure to flood risk has been studied in this work. Historically, more than 300 floods have been recorded in the area, leading to remarkable economic losses (Ivanov et al., 2013). To protect the city from floods, in 1978, the Council of Ministers of the Union of Soviet Socialist Republics (USSR) approved a hydraulic engineering construction project named St. Petersburg Flood Prevention Facility Complex (FPFC). The project began in 1979 and after a long period of construction, it was finally completed in 2011. As the complex plays a crucial role in resisting floods, its structural stability is a public concern. The structure extends for 25.4 km and traditional point-based monitoring practices (such as levelling or GPS) are too expensive to be regularly implemented (Badenko et al., 2018; Fedorov et al., 2016) and conversely, the MT-InSAR techniques turn out to be very useful in monitoring the dams (Milillo et al., 2016; Neokosmidis et al., 2016; Shi et al., 2015; Zhao et al., 2017).

The main goal of our investigation was to characterise the current stage of deformations in St. Petersburg. To achieve this task, the MT-InSAR (Berardino et al., 2002) technique, adequately complemented with the MinA approach (Pepe et al., 2016), has been exploited to recover the temporal evolution of the 2-D ground deformation.

2. Study area

St. Petersburg is the second-largest city in Russia. It is situated on the shores of the Neva River, at the head of the Gulf of Finland in the Baltic Sea (Fig. 1b). It is the northernmost city, with a population of more than one million and is also known as the "Northern Capital" of Russia. The topography of St. Petersburg is mostly flat and the elevation ranges approximately between 1–2 m above sea level (Fig. 1c). Due to the shallowness of the Neva Bay, the flatness of its bottom, and the narrowing of the Gulf of Finland within the Neva Delta (Fig. 1a), the coastal area of St. Petersburg has suffered from frequent floods, notably when storm surges have coincided with regular high tides (Kosukhin et al., 2015). Historically, more than 300 floods have occurred since 1703 (Kosterin and Shchekachikhin, 2017) and the municipal government designed the St. Petersburg Flood Prevention Facility Complex to prevent the city from being flooded.

3. Data and methodology

3.1. Sentinel-1 SAR data

Two independent SAR datasets (from Sentinel-1A (S-1A) and Sentinel-1B (S-1B)) were used to investigate the land subsidence in the St. Petersburg area. The first dataset consisted of 65 SAR images, acquired by the C-band S-1A/B sensors on their ascending orbits from 28 May 2016 to 22 August 2018. The second SAR dataset was collected along the descending paths, from 16 May 2016 to 22 August 2018 and consisted of 64 SAR images. All the SAR data were acquired in the interferometric wide swath (IW) mode. The temporal distributions of the available S-1A/B SAR datasets for both the ascending and descending data tracks are shown in Fig. 2.

3.2. Generation of line-of-sight surface deformation time series

The ground deformation in the St. Petersburg area was recovered by processing the two available SAR datasets using the Small BAseline Subset (SBAS)[1] algorithm (Berardino et al., 2002), thus obtaining, corresponding to a set of very coherent points, the relevant LOS-projected deformation time series. To this aim, the sets of small baseline (SB) interferometric data pairs were firstly selected by imposing a maximum temporal baseline of 90 days. The chosen interferometric data pairs are shown in the temporal/perpendicular baseline domain as connecting lines between the SAR acquisitions (Fig. 3). An ASTER GDEM of the area (30 m resolution) has been used to flatten the differential interferometric phases. For both the data-sets, the highly coherent points were selected by identifying those pixels that exhibit a mean coherence value larger than 0.55. Over these pixels, the subsequent phase unwrapping step, relying on the application of the Minimum Cost Flow unwrapping technique (Costantini, 1998), was performed to get the full (unrestricted to the measured $[-\pi,\pi[$ interval) differential phases. The modified version of the multi-track MinA combination technique was then applied to decompose the independently obtained LOS surface deformation time series into the relevant Up-Down and East-West ground deformation time series.

3.3. Minimum acceleration (MinA) combination technique

The MinA combination algorithm is a post-processing tool developed for retrieving the time series of 3-D deformation by linking the information in the LOS-projected deformation of the Earth's surface retrieved by complementary SAR viewing angles (Pepe et al., 2016). The main benefits of the MinA algorithm are: i) the possibility to combine, in a post-processing stage, different radar LOS-projected deformation measurements and ii) the potential to discriminate the 3-D deformation time series with enhanced (concerning that of the single LOS measurements) temporal sampling. The only requirement is that the SAR data must have a suitable temporal overlap and must be acquired at complementary viewing angles (e.g., through ascending and descending flight passages).

Unlike the original MinA algorithm (Pepe et al., 2016) that focused on obtaining 3-D deformation products, we here introduce some simplifications to compute only the deformation time series of the Up-Down and East-West (2-D) components. Indeed, due to the near-polar orbit satellite configuration, the accuracy of the North-South deformation measurements is on the order of a few centimetres. Accordingly, the sensitivity of North-South measurements results are not adequate for areas such as St. Petersburg, where the deformation signals are less prominent. The adopted simplification is based on the assumption that the contribution of the North-South deformation to the LOS-projected deformation signals is negligible.

In the following sections, the rationale of the simplified MinA algorithm is summarised. We assumed the availability of N complementary datasets of SAR images acquired at different viewing geometries and considered each dataset as composed of Q_i $(i = 1, 2, ..., N)$ SAR acquisitions. Starting from these images, the LOS-projected

[1] The ENVI's SARscape modules have been applied.

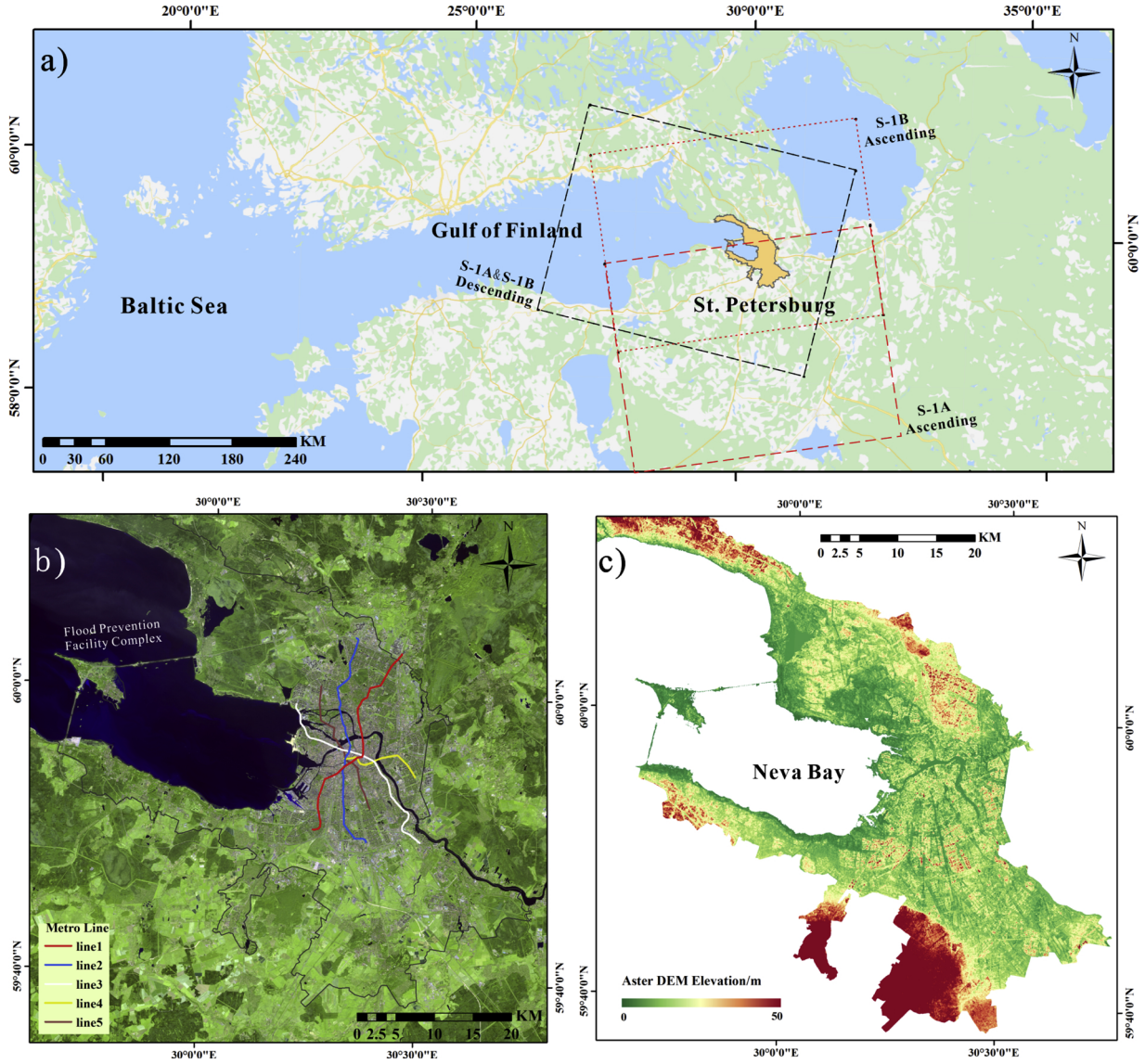

Fig. 1. a) Location of St. Petersburg, the tracks of the ascending and descending Sentinel-1A/B (S-1A/B) are depicted by the red and black dotted rectangles, respectively. b) Landsat-8 image collected on 2 May 2017. Location of the Flood Prevention Facility Complex (FPFC) is highlighted and the metro lines are plotted. c) The Advanced Spaceborne Thermal Emission and Reflection Radiometer Global Digital Elevation Model (ASTER GDEM) of St. Petersburg (30 m ground resolution, version 2, released in 2011).

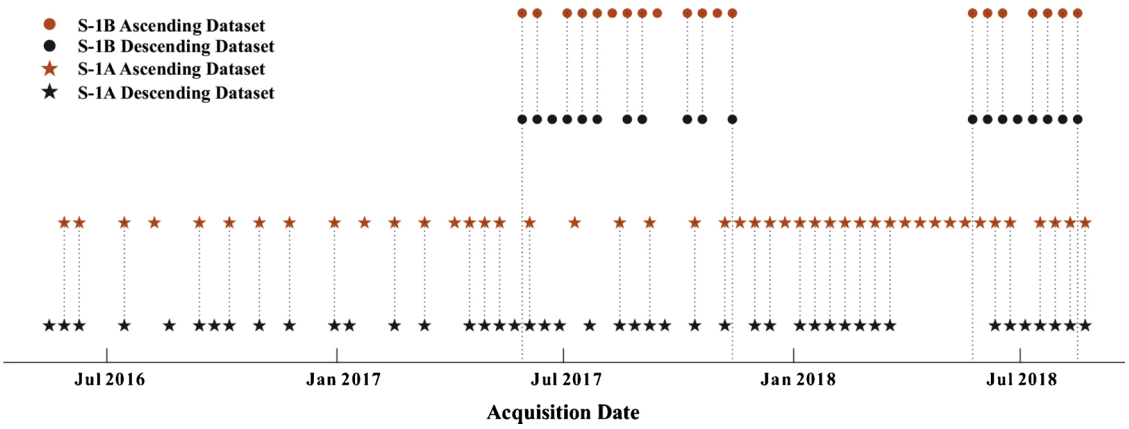

Fig. 2. Temporal distribution of S-1A/B datasets used in this study.

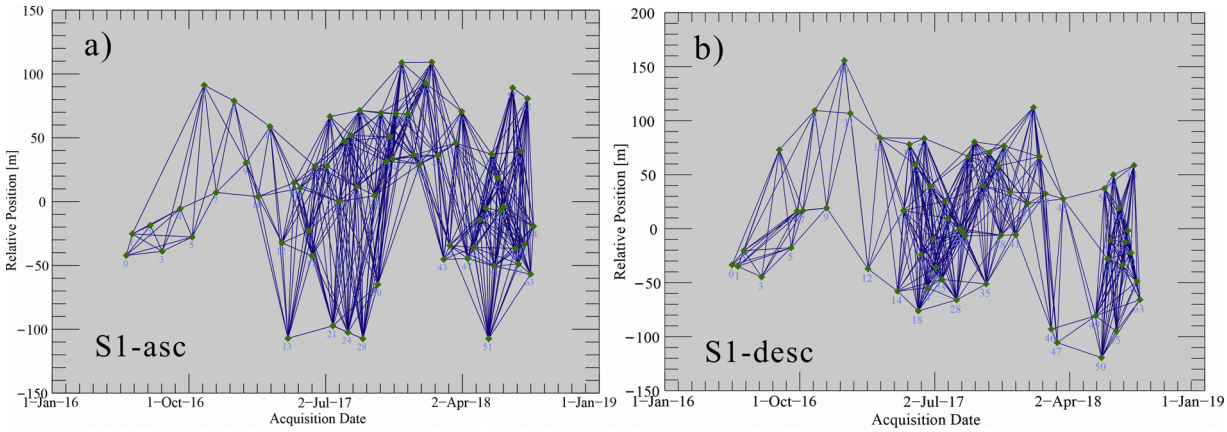

Fig. 3. Distribution of the S-1A/B ascending (a), and descending (b) interferometric SAR data pairs in the temporal/perpendicular baseline plane. The SAR acquisitions are represented by diamonds and the connecting arcs correspond to the selected interferometric SAR data pairs.

deformation time series related to every dataset, namely $\boldsymbol{d^i_{LOS}} = [d^i_1, d^i_2, d^i_3, ...d^i_{Q_i}]$ $(i = 1, 2, ..., N)$, are independently generated and geo-referenced to a common geographical spatial grid, where the subsequent multi-satellite combination technique is applied. Acquisition dates related to every SAR dataset are described as $\boldsymbol{T^i} = [t^i_1, t^i_2, t^i_3, ...t^i_{Q_i}]$ $(i = 1, 2, ..., N)$. The ordered dates of all SAR datasets are expressed as $\boldsymbol{T} = [T_1, T_2, T_3, ..., T_Q]$, where Q represents the whole number of available SAR images[2] . According to the geometric relationship based on satellite imaging (Fig. 4) and neglecting the contribution of deformation along the North-South (N-S) direction, we can decompose the radar LOS-projected surface deformations along the East-West and Up-Down directions as follows:

$$\begin{aligned} d_{LOS,asc} &= \sin\theta_{asc} \bullet d_{East-West} + \cos\theta_{asc} \bullet d_{Up-Down}, \\ d_{LOS,desc} &= -\sin\theta_{desc} \bullet d_{East-West} + \cos\theta_{desc} \bullet d_{Up-Down} \end{aligned} \quad (1)$$

where θ_{asc} and θ_{desc} are the local incidence angles of the transmitted electromagnetic waves on the ground (Franceschetti and Lanari, 1999) for the ascending and descending data tracks, respectively, and and $d_{Up-Down}$ are the deformations in the East-West and Up-Down directions, respectively. The MinA technique implies a pixel-by-pixel temporal analysis; accordingly, the dependence of the algorithm on the spatial variables is not explicitly mentioned hereafter.

Following the same lines detailed in Pepe et al. (2016), we could write a system of $Q - N$ linear equations with respect to the $2(Q - 1)$ unknowns, namely $\boldsymbol{V_{East-West}}$ and $\boldsymbol{V_{Up-Down}}$, which represent the East-West and Up-Down velocities among the contiguous dates, as follows:

$$\boldsymbol{B} \bullet \begin{bmatrix} \boldsymbol{V_{East-West}} \\ \\ \boldsymbol{V_{Up-Down}} \end{bmatrix} = \begin{bmatrix} \boldsymbol{d^1_{LOS}} \\ \boldsymbol{d^2_{LOS}} \\ \vdots \\ \boldsymbol{d^N_{LOS}} \end{bmatrix} \quad (2)$$

with:

$$\boldsymbol{B} = \begin{bmatrix} \boldsymbol{B}^1\sin\theta^1 & \boldsymbol{B}^1\cos\theta^1 \\ \boldsymbol{B}^2\sin\theta^2 & \boldsymbol{B}^2\cos\theta^2 \\ \vdots & \vdots \\ \boldsymbol{B^N}\sin\theta^N & \boldsymbol{B^N}\cos\theta^N \end{bmatrix} \quad (3)$$

More specifically, to build the matrix $\boldsymbol{B^i}$ (Berardino et al., 2002), the duration of the time intervals between the consecutively ordered time acquisitions has to be taken into account. In particular, if we consider the *i-th* SAR dataset and refer to the related deformation time series vector, namely $\boldsymbol{d^i_{LOS}} = [d^i_1, d^i_2, d^i_3, ...d^i_{Q_i}]$, the *j-th* LOS-projected deformation value can be calculated as:

$$\begin{aligned} d^i_j = &\sum_{k=1}^{IE^i_j} (T_{k+1} - T_k) \bullet v_{East-West,k} \bullet \sin\theta^i \\ &+ \sum_{k=1}^{IE^i_j} (T_{k+1} - T_k) \bullet v_{Up-Down,k} \bullet \cos\theta^i, \\ &j = 1,2,...,Q_i \; i = 1,...,N \end{aligned} \quad (4)$$

where IE^i_j is the index of the *j-th* ordered time acquisitions related to the *i-th* SAR dataset with respect to the whole ordered time vector $\boldsymbol{T}$, where $\Delta\boldsymbol{T_k} = T_{k+1} - T_k \; k = 1, 2, ..., Q - 1$ and θ^i represents the local incidence angle of the transmitted electromagnetic waveform from the *i-th* radar sensor location on the ground for the given target. To solve the problem, Eq. (2) is subsequently regularised by imposing the condition that the (unknown) 2-D (East-West, Up-Down) deformation time series at the given SAR pixel location have a minimum acceleration (Pepe et al., 2016). This condition is obtained by adding the following equations:

$$\boldsymbol{C} = \begin{cases} \delta(v_{E_{i+1}} - v_{E_i}) = 0 \;\; i = 1, ..., \; Q - 2 \\ \delta(v_{U_{i+1}} - v_{U_i}) = 0 \;\; i = 1, ..., \; Q - 2 \end{cases} \quad (5)$$

where δ is a regularisation factor that is needed to balance the weight of the minimum acceleration and the minimum residual norm constraints of the system of Eq. (3). The regularised system of linear equations could then be re-written as:

$$\begin{bmatrix} \boldsymbol{B} \\ \boldsymbol{C} \end{bmatrix} \bullet \begin{bmatrix} \boldsymbol{V_{East-West}} \\ \\ \boldsymbol{V_{Up-Down}} \end{bmatrix} = \begin{bmatrix} \boldsymbol{d^1_{LOS}} \\ \boldsymbol{d^2_{LOS}} \\ \vdots \\ \boldsymbol{d^N_{LOS}} \\ 0 \end{bmatrix} \quad (6)$$

The system of Eq. (6) can be solved in the least-squares (LS) sense with respect to the 2-D (East-West, Up-Down) (unknown) deformation velocity components, $\boldsymbol{V_{East-West}}$ and $\boldsymbol{V_{Up-Down}}$. Finally, the East-West and Up-Down deformation time series are computed by time integration (pixel by pixel) of the obtained 2-D deformation velocity components.

3.4. Error budget of the two-dimensional ground deformation time series

This section provides an analysis of the accuracy of the 2-D round deformation time series obtained using the MinA algorithm. Considering a single SAR dataset composed of $N + 1$ SAR images and M differential interferograms, let $[\psi_1, \psi_2, ..., \psi_M]^T$ be the M SB differential SAR interferograms. The standard deviation of the phase noise can be calculated as (Tough et al., 1995):

[2] Note that T_i is expressed as "fractions" of a day to deal with the problem of quasi-simultaneous SAR scenes in the high-latitude areas.

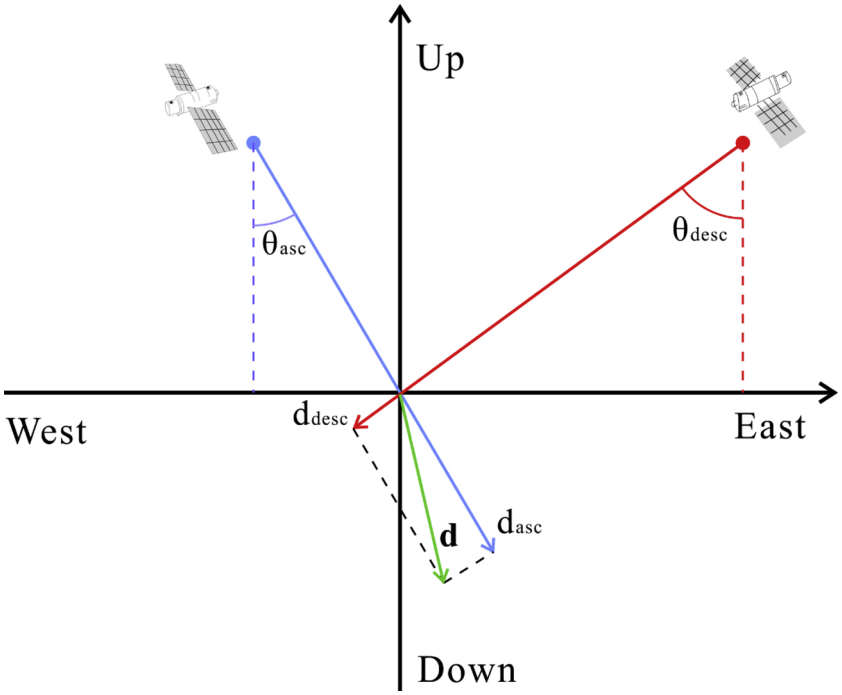

Fig. 4. Sketch of the SAR observations geometries as seen from the ascending (in blue) and descending (in red) orbits.

$$\sigma_k^2 = var(\psi_k) \cong \frac{1-\gamma_k^2}{2L\gamma_k^2}, \quad k = 1,\ 2,\ ...,M \tag{7}$$

where $L$is the number of looks used to perform the multi-looking operations and γ_k is the coherence of the *k-th* differential interferogram at the given location of the generic radar pixel. Assuming that the interferometric signals are statistically independent and identically distributed (with standard deviations as in Eq. (7)), the covariance matrix of the interferograms is:

$$\boldsymbol{C}_{\psi} = \begin{bmatrix} \sigma_1^2 & 0 & ... & 0 \\ 0 & \sigma_2^2 & ... & 0 \\ ... & ... & ... & ... \\ 0 & 0 & ... & \sigma_M^2 \end{bmatrix} \tag{8}$$

Assuming that the interferograms form a unique subset of data[3], the SBAS inversion turns out in a simpler Least-squares inversion, that is to say:

$$\boldsymbol{\phi} = \boldsymbol{I_g}\boldsymbol{\psi} \tag{9}$$

where $\boldsymbol{\phi}$ is the series of the phases associated with every single SAR image. $\boldsymbol{I_g}$ is the generalised inverse of the incidence-like matrix of the interferometric data pairs (Berardino et al., 2002) and $\boldsymbol{\psi}$ is the vector of the interferograms. At this stage, the error propagation theory (Draper and Smith, 1988) states that the covariance matrix of the computed deformation time series $\boldsymbol{\phi}$ is as follows:

$$\boldsymbol{C_{\phi}} = \boldsymbol{I_g}\boldsymbol{C_{\psi}}\boldsymbol{I_g^T} \tag{10}$$

But the deformation is related to the phase as $\mathbf{d}_{\boldsymbol{LOS}} = \frac{\lambda}{4\pi}\boldsymbol{\phi}$. Accordingly, the covariance matrix of the LOS-projected deformation time series is:

$$\boldsymbol{C_{d_{LOS}}} = \left(\frac{\lambda}{4\pi}\right)^2 \boldsymbol{I_g}\boldsymbol{C_{\psi}}\boldsymbol{I_g^T} \tag{11}$$

To estimate the covariance matrix of the reconstructed East-West and Up-Down deformation time series, first, the covariance matrices of the single LOS-projected deformation time series are computed as in Eq. (11) and the error propagation rules are then applied to the solution of Eq. (6), which can be reformulated as follows:

$$\mathbf{V} = \begin{bmatrix} \boldsymbol{V_{East-West}} \\ \boldsymbol{V_{Up-Down}} \end{bmatrix} = \boldsymbol{\Lambda} \begin{bmatrix} \boldsymbol{d_{LOS}^1} \\ \boldsymbol{d_{LOS}^2} \\ \vdots \\ \boldsymbol{d_{LOS}^N} \end{bmatrix} \tag{12}$$

where N is the number of available independent SAR datasets to be combined and $\boldsymbol{\Lambda}$ is the generalised inverse matrix of matrix $\begin{bmatrix} \boldsymbol{B} \\ \boldsymbol{C} \end{bmatrix}$ in the Eq. (6). As a result, we have:

$$\begin{aligned} \boldsymbol{C_V} &= \begin{bmatrix} \boldsymbol{C_{V_{East-West}}} & \boldsymbol{C_{V_{East-West},V_{Up-Down}}} \\ \boldsymbol{C_{V_{Up-Down},V_{East-West}}} & \boldsymbol{C_{V_{Up-Down}}} \end{bmatrix} \\ &= \boldsymbol{\Lambda} \begin{bmatrix} \boldsymbol{C_{d_{LOS}^1}} & 0 & ... & 0 \\ 0 & \boldsymbol{C_{d_{LOS}^2}} & ... & 0 \\ ... & ... & ... & ... \\ 0 & 0 & ... & \boldsymbol{C_{d_{LOS}^N}} \end{bmatrix} \boldsymbol{\Lambda^T} \end{aligned} \tag{13}$$

However, the East-West and Up-Down deformation time series are obtained by time integration of the vectors $\boldsymbol{V_{East-West}}$ and $\boldsymbol{V_{Up-Down}}$. Thus, after trivial mathematical manipulations, we get:

$$\boldsymbol{C_{d_{EW}}} = \boldsymbol{\Omega}\boldsymbol{C_{V_{East-West}}}\boldsymbol{\Omega^T} \tag{14}$$

where :

$$\boldsymbol{\Omega} = \begin{bmatrix} T_2 - T_1 & 0 & ... & 0 \\ T_2 - T_1 & T_3 - T_2 & ... & 0 \\ ... & ... & ... & ... \\ T_2 - T_1 & T_3 - T_2 & ... & T_Q - T_{Q-1} \end{bmatrix}$$

and, similarly, for the Up-Down deformation time series, we have:

$$\boldsymbol{C_{d_{UD}}} = \boldsymbol{\Omega}\boldsymbol{C_{V_{Up-Down}}}\boldsymbol{\Omega^T} \tag{15}$$

[3] The extension of the presented calculations in the case of more than one subset is a matter for future investigations.

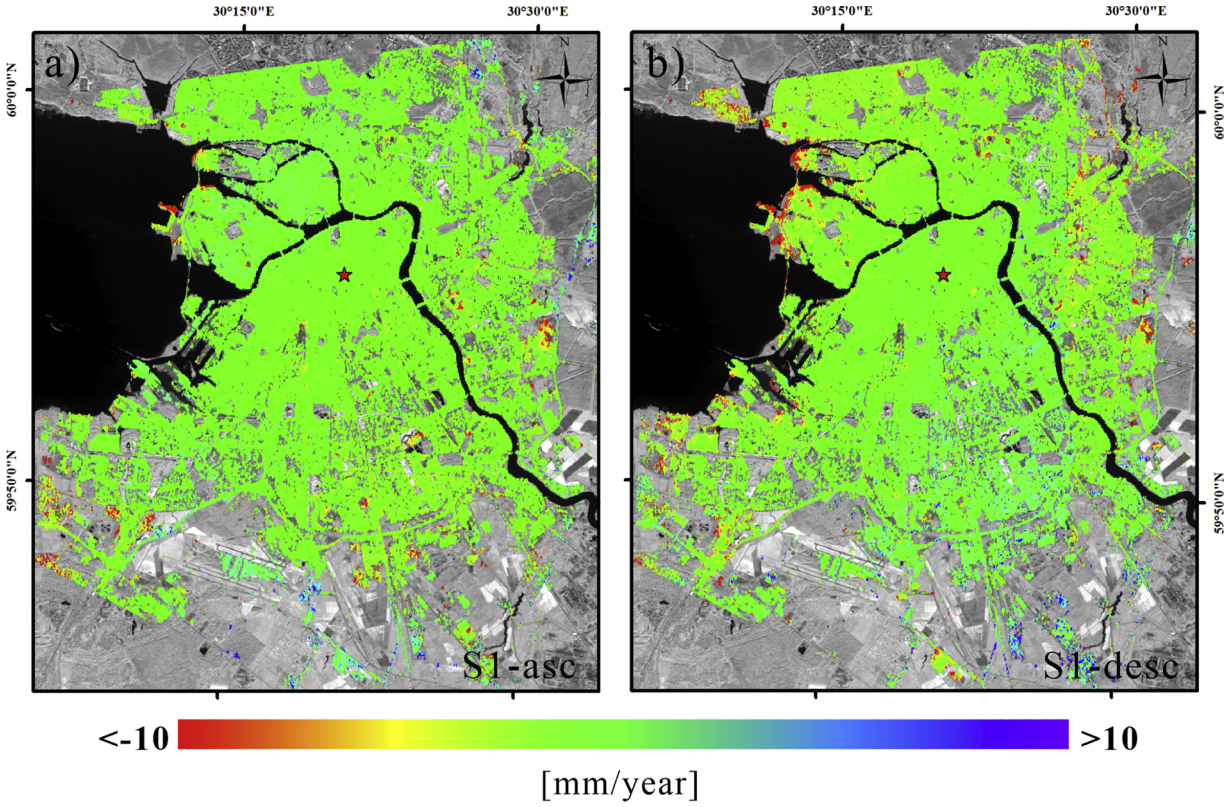

Fig. 5. St. Petersburg city centre area. Geocoded mean LOS deformation velocity maps, retrieved by the S-1A/B ascending (a) and descending (b) tracks. The red star in the figure represents the location of the reference point.

4. Results

4.1. Line-of-sight-projected deformation time series

The SBAS algorithm has been applied for the retrieval of the LOS-projected deformation time series for both the ascending and descending S-1A/B SAR datasets. The deformation time series were calibrated to a relatively stable common reference point (the location is highlighted by the red star in Fig. 5), where the deformation was assumed zero. Fig. 5a and b show the LOS-projected mean deformation velocity maps for the ascending and descending data tracks, respectively.

Evidently, most parts of the St. Petersburg city centre are rather stable, except for the western coastal area of the Neva delta, where the deformation could be correlated to the land reclamation project that was conducted in the area. With the help of three historical Landsat images, the land reclamation map (Fig. 6) of St. Petersburg was generated. More precisely, both the base image acquired in 1996 and that collected in 2010 were taken by the Landsat-5 Thematic Mapper (TM) sensor, whereas the last image was acquired in 2018 by the Landsat-8 Enhanced Thematic Mapper (ETM+). All the images were captured during a relatively low tide condition. Most of the subsidence areas in the western coastal region are areas that were reclaimed in the recent decades (Fig. 6) and a maximum subsidence rate of about 20 mm/year has been measured.

4.2. Generation of two-dimensional deformation time series

To retrieve the 2-D (Up-Down and East-West) deformation time series of the St. Petersburg area, the LOS-projected deformation time series were first geocoded to the same reference grid of pixels (consisting of 553,096 points) and the simplified MinA algorithm was applied.

The mean deformation velocity maps of the Up-Down and East-West surface deformations are shown in Fig. 7a and b, respectively.

Six ground points, labelled as I-VI, have been pre-selected (Fig. 7b) and the corresponding Up-Down and East-West deformation time series are plotted in Fig. 8. The error bars for the obtained deformation time series, computed by applying the statistical analysis outlined in Section 3, are shown in Fig. 8. The deformation signals along the Up-Down direction are predominant compared with the corresponding deformation signals recorded along the East-West direction. This finding confirms the fact that the land reclamation processes are responsible for the subsidence phenomena. It is also worth noting that the possibility to monitor both the East-West and Up-Down movements with increased temporal sampling is of high relevance. In particular, the ground displacement signals observed in the South-West area (Fig. 7) are likely due to presence of facilities for the production of biogas; these areas are now under urban renewal and infill. In the following section, the accuracies of the generated East-West and Up-Down deformation time series are addressed. As expected, the accuracy of the Up-Down deformation components is better than that of the East-West deformation components and it improves as the average spatial coherence of the selected pixels increases. In particular, the points I and II that are located in the reclamation areas, show a clear, time-linear subsidence trend, with a maximum cumulative deformation of about 4 cm. In some time-dependent models that describe deformation processes over land-reclaimed areas (for instance, Zhao et al., 2015; Plant et al., 1998), the deformation exhibits a somewhat non-linear temporal dependence. Specifically, these ground deformation models typically have a temporal exponential decay behaviour, characterised by high subsidence trends during the first stages after the end of the reclamation procedures, followed by a progressive reduction of the deformation rate until a stable condition is eventually reached. Since the observed deformation signals in the area of St. Petersburg are mostly linear in the observed time period (2016–2018), we could assume that the soil

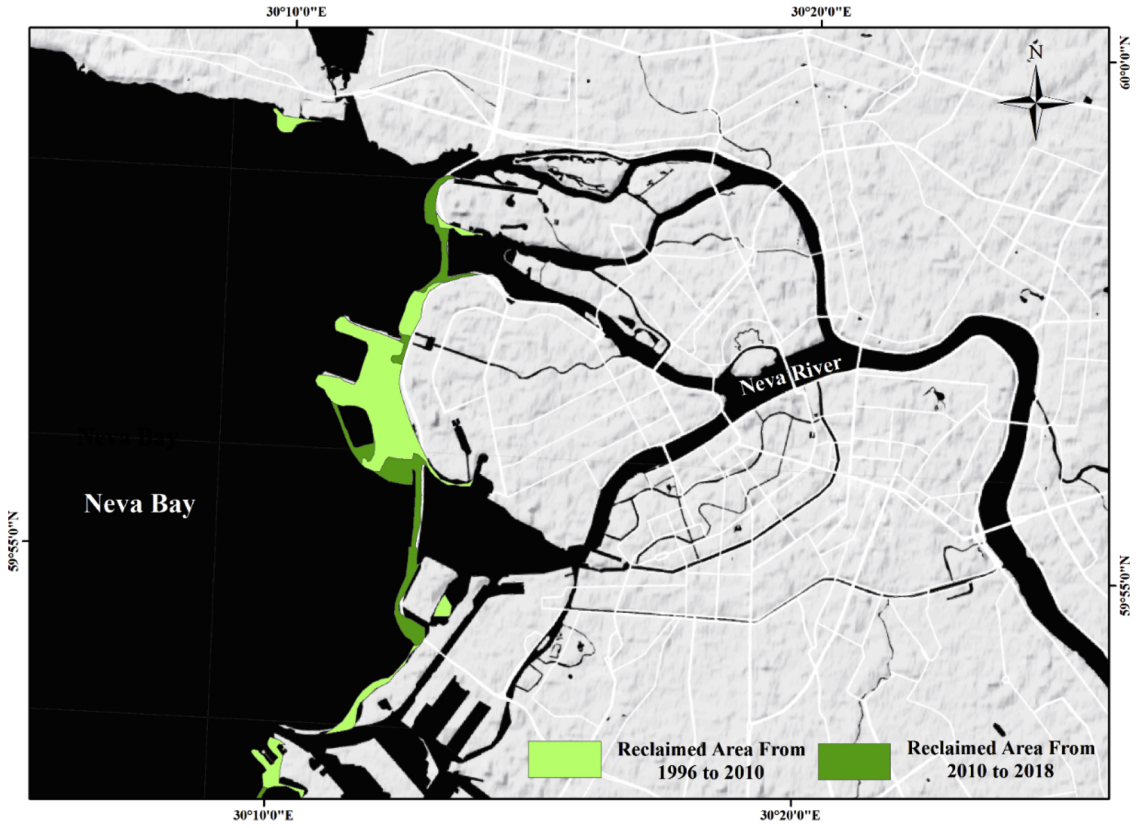

Fig. 6. Distribution of land reclamation area in St. Petersburg, Russia, based on three Landsat images acquired in 1996 (Landsat-5), 2010 (Landsat-5), and 2018 (Landsat-8), respectively.

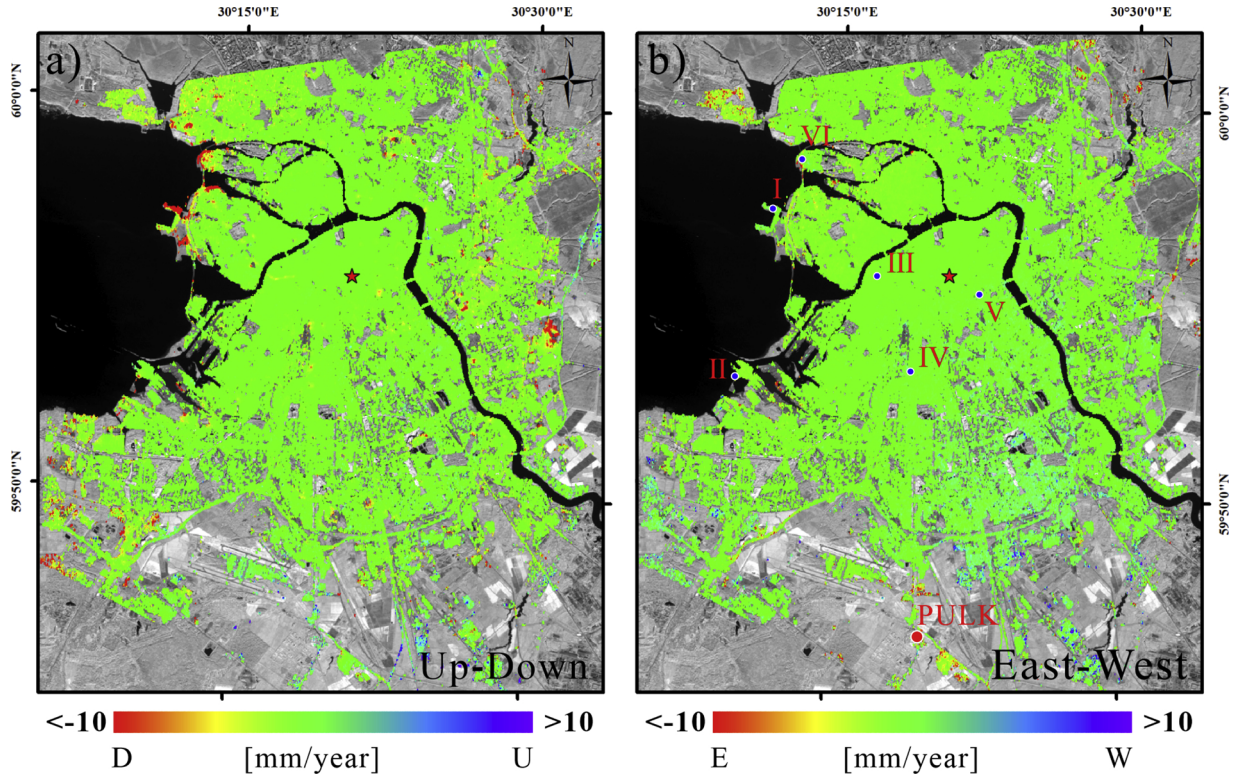

Fig. 7. Geocoded Up-Down (a) and East-West (b) mean deformation velocity maps of the city centre area for 2016–2018. The selected points, labelled as I-VI, are identified in the map (b) with blue circles. The red point labelled as PULK is a GPS station.

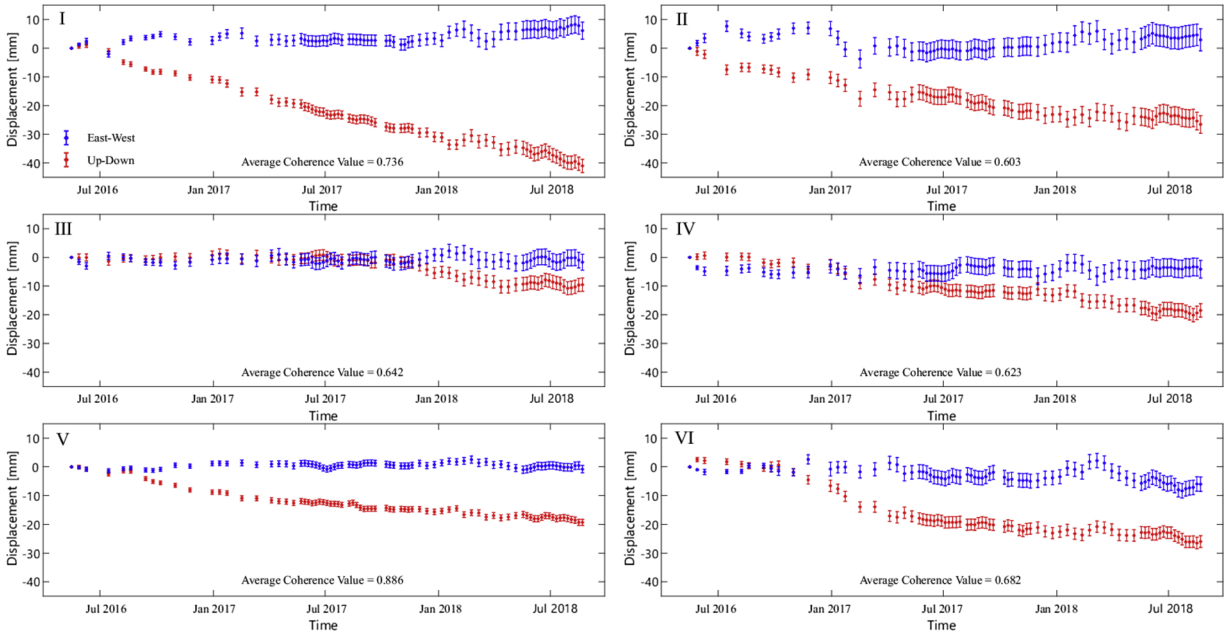

Fig. 8. East-West (blue points) and Up-Down (red points) deformation time series of six ground points labelled as (I-VI) in Fig. 7b; the theoretical error bar of each point is also depicted.

consolidation phase is still in progress. Accordingly, the terrain might continue to be subjected to subsidence in the next few years. Further analyses are required to confirm the validity of this outcome. Conversely, the ground deformation time series of points III-VI that are located in correspondence with the metro line tunnels and stations, could be described as caused by different ground deformation mechanisms.

Currently, in the city centre, there are five metro lines under operation, with a total mileage of 113.5 km in 2017. The city is built on marshland that consists of water-saturated soils; loam, sand, and peat bogs. Considering the geological conditions of the investigated area as well as the dense distribution of the river network, most of the subway stations were built at great depths (Filippova and Matyushina, 2016). For instance, the depth of the “Admiralteyskaya” (Адмиралтейская) station of the Metro Line 5 reaches 86 m, making it the deepest subway station in the world. A significant water permeation accident occurred on the Metro Line 1 in 1995, rendering the tunnels between the "Lesnaya" (Лесная) and the "Ploschad Muzhestva" (ПлощадьМужества) stations unusable. For all these reasons, an investigation of the current stage of ground deformation along the entire metro line network is of high relevance for urban planners and security practitioners. In our study, we have extracted the Up-Down deformation time series of all the coherent points within a radius of 500 m from the positions of the metro line network on the ground. Fig. 9a shows the map of the Up-Down mean deformation velocity.

As most of the tunnels of the subways in St. Petersburg exist at great depths, there is no significant subsidence along the metro lines, except in the Primorskaya to Begovaya section of Line 3 and in some areas near the subway stations of Lines 2 and 4 (Fig. 9a). The section between the Primorskaya and the Begovaya stations was built very recently because Russia hosted the 2018 World Cup, and the tunnels were constructed near Neva Bay. In particular, analysis of the Up-Down deformation time series of Point VI that is located in the proximity of the tunnel revealed that most of the deformations occurred before January 2018. Subsequently, the subsidence velocity has become moderate (i.e., the mean subsidence velocity from May 2016 to January 2018 is 13 mm/year and from January 2018 to August 2018 is 5 mm/year). Furthermore, a ground subsidence signal was discovered along the extension of Line 4 near the banks of the Neva River. From the analysis of the Up-Down deformation time series of Point III, it could be argued that the ground surface was stable during the early stage, after which it underwent accelerated subsidence. The area of Line 4, wherein Point III is located, is geologically fragile and is subjected to ground deformation and soil liquefaction risks due to the fine-grained lithology of the Quaternary deposits (Fig. 9b). As shown in the geological section of Fig. 9c, the Quaternary deposits near the Neva River are much thicker than those inland and the deposits have high moisture content, due to the long-time soaking in the river water. It made this area more susceptible to the soil compaction mechanisms under the construction of the metro tunnel and finally led to the observed ground displacements. Moreover, some areas near the Ligovskiy Prospekt, Elektrosila, and Kupchino stations have also been affected by the ground subsidence phenomena due to the underground construction of the subway stations. In particular, in the Begovaya station, Terminal 3, which was opened on 26 May 2018, an evident annular settling funnel appeared, reaching a maximum subsidence rate of about 12 mm/year.

Preliminary cross-validation of the obtained InSAR results with the external ground terrain displacement measurements has been performed. Unfortunately, due to policy restrictions of the Russian government, the GPS and levelling measurements are not freely available, except for two GPS stations located south of the study area, for which the ground deformation measurements were downloaded from the website: http://geodesy.unr.edu/NGLStationPages/gpsnetmap/GPSNetMap.html (Blewitt et al., 2018). Specifically, the location of the available GPS station, labelled as PULK, is highlighted in Fig. 7 by a red point. We compared the estimated ground displacement at PULK with the Up-Down and East-West ground terrain displacements time series (Fig. 10). The root mean square errors (RMSEs) of the differences between the InSAR derived displacements and the GPS measurements are 3.7 mm and 2.6 mm for the Up-Down and the East-West deformation components, respectively.

5. Flood risk in the St. Petersburg Area

Long-term and persistent occurrence of floods has placed demands on the stability of the St. Petersburg Flood Prevention Facility Complex. This section will provide information about flood events that St. Petersburg has encountered in the past and the present stage of structural deformation of the FPFC using the MinA combination algorithm.

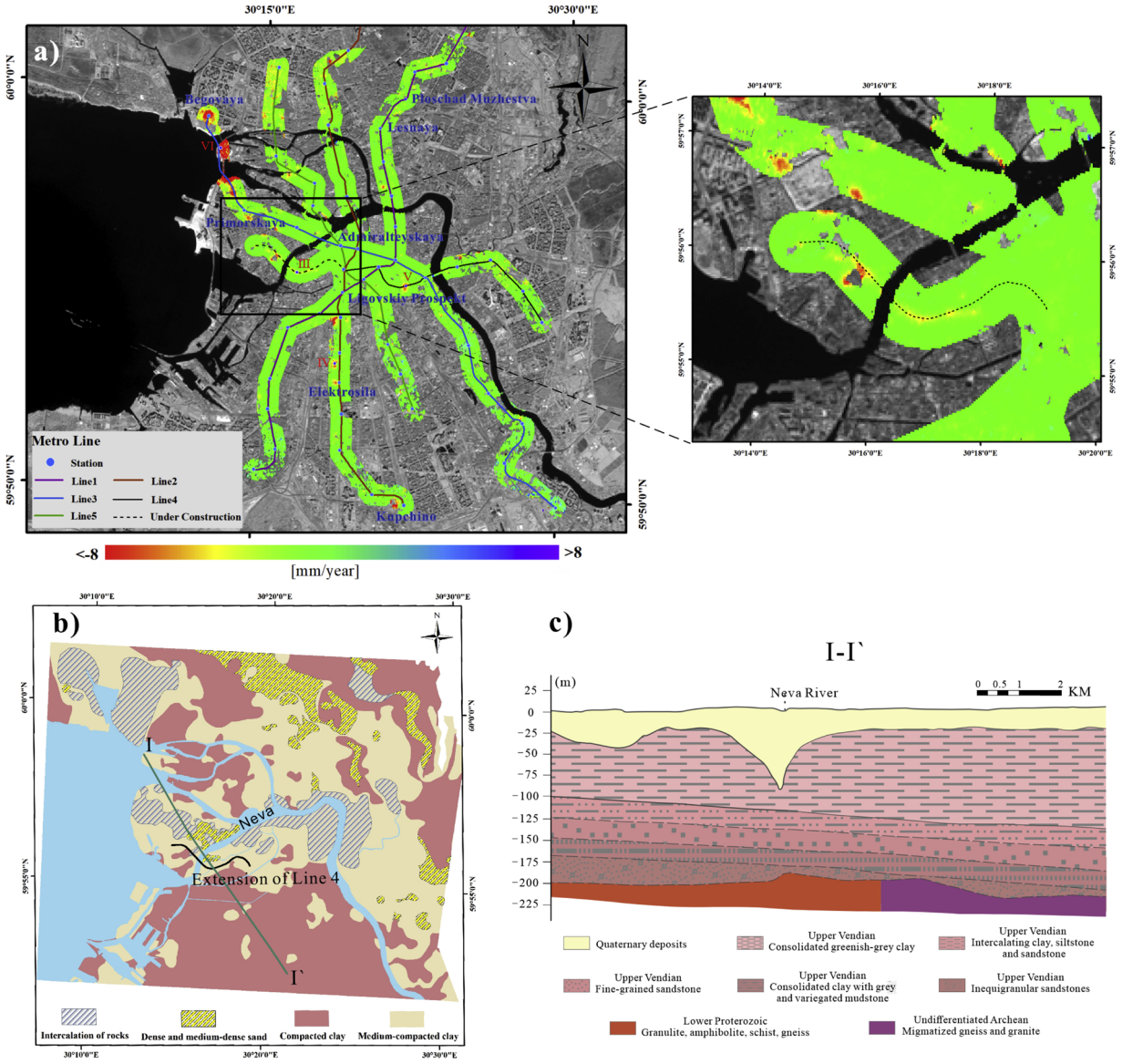

Fig. 9. a) Map of the Up-Down mean deformation velocity retrieved using the S-1A/B combined deformation time series from 2016 to 2018 and the buffer of metro lines. b) Engineering geological map of the St. Petersburg city centre and c) Geological section of the profile line I-I` depicted in (b), partially referring to Philippov and Spiridonov (2009).

5.1. *Historical floods*

From 1703 to 2010, a total of 339 flood events have been recorded, out of them, three were catastrophic; especially the flood in 1824 when the water rose up to 421 cm and killed hundreds of people. Analysing the historical records of the tides, we found that 86 % of the floods occurred during the period from September to January (Fig. 11). This could be attributed to the prevailing westerly winds in the Baltic Sea,

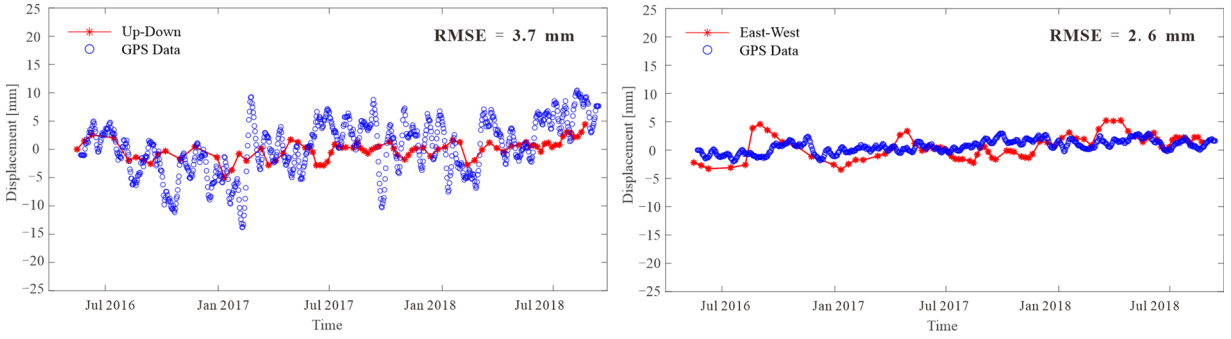

Fig. 10. Two-Dimensional Up-Down and East-West deformation time series of the GPS site PULK as recorded by the GPS and calculated from the presented InSAR analysis.

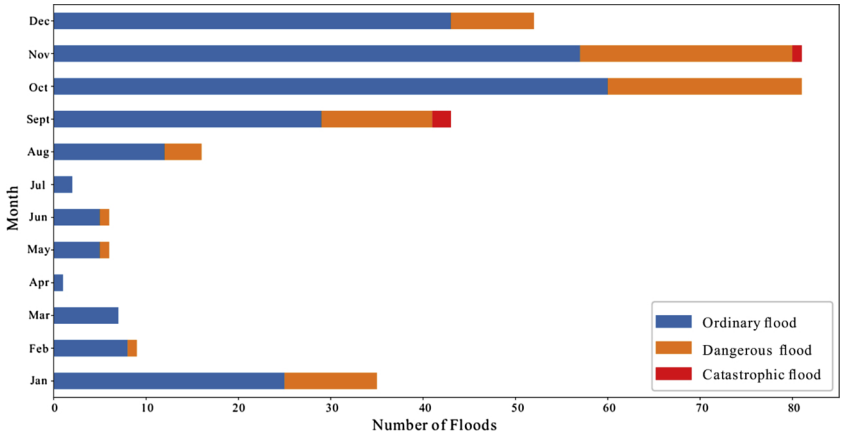

Fig. 11. Monthly counts of historical floods. All floods are categorised into three levels of hazard: Ordinary floods (water level between 160–210 cm), dangerous floods (water level between 210–300 cm), and catastrophic floods (water level higher than 300 cm).

especially in autumn and winter that cause the ocean currents to flow into the narrow Gulf of Finland, finally leading to the rising of water level and urban flooding. Historical data show that between 1703 and 1975, 263 flood events have been recorded, with a rate of approximately one flood per year, and from 1975 to 2010, 75 flood events have occurred, at a rate of about two flooding events per year, which is twice compared with the previous period of observation. Quality of the historical data is expected to be definitely lower than the recent measurements. However, the archives of data show that the risk of flooding in the city area of St. Petersburg has continuously been high during the last centuries and extreme events have been threatening the populations.

5.2. St. Petersburg flood prevention facility complex

The FPFC is a 25 km long dam that was constructed to prevent flooding and to facilitate transportations. Its construction began in 1979 and was suspended in the 1990s due to the Russian economic downturn. At the beginning of the 21 st century, the work was recommenced and finally completed in 2011. The dam is divided into 11 sections (D1-D11) by six sluices (B1-B6) and two navigation openings (S1 and S2); usually the openings are used to allow shipping access and are closed when there is a risk of flooding. The structure was first used on 28 November 2011 to hold back the entry of the Baltic Sea water into the Neva Bay. By 2018, more than 10 potential floods were blocked by the complex. As it plays such an essential role in flood prevention, monitoring the stability of the complex is crucial for public safety. The MT-InSAR techniques guarantee large-scale coverage and repeatability. Fig. 12a shows the map of LOS-projected mean deformation velocity of the dam for the period of 2016–2018, as revealed by the S-1A/B descending data. The complex is generally stable, except for the D3 section, which has a maximum subsidence velocity of 12 mm/year. Unfortunately, the available ascending SAR data does not cover region over the entire dam, except for the one year of observations from 2017 to 2018. Nonetheless, the South-Western (SW) sector of the dam is covered by both the ascending and descending flight passes. Thus, we computed the East-West and the Up-Down deformation time series of the SW sector by applying the simplified MinA approach. Fig. 12b and c show the mean deformation velocity of the Up-Down and East-West ground movements across the dam. The deformation is concentrated mostly at the D3 section and a sensible lateral deformation of the structure has also appeared. Fig. 12d and e show the maps of the RMSE between the measured displacement and the deformation rates, respectively for the Up-Down and the East-West displacements. Across the entire structure, the RMSE is about 2 mm for the East-West deformation components and about 1.5 mm for the Up-Down ones. Fig. 12a shows that the lithology of both sides of the D3 section (Philippov and Spiridonov, 2009) is different. This might result in distinct surface bearing capacities on the two sides and eventually, causes the observed differential (lateral) movement of the dam. Furthermore, the difference between the water-load on both sides of the barrier could be another reason. The vast Neva Bay has gradually slowed down the velocity of the Neva River and the water becomes mostly stationary when it reaches the eastern part of the dam after flowing for several tens of kilometres. On the contrary, the western part of the barrier could continuously be suffering enormous pressure from the ocean currents from the Baltic, especially during autumn and winter, when the current coincides with prevailing westerly winds in the Baltic Sea.

6. Conclusion

We have investigated the ground deformation in St. Petersburg and its surrounding areas, using an advanced multi-track InSAR technique, applied to two sets of S-1A/B data collected over the investigated regions from May 2016 to August 2018. The SBAS algorithm complemented by a simplified version of the MinA combination technique has been used for this study. The 2-D East-West and the Up-Down ground deformation time series in correspondence with the high-coherent SAR pixel locations have been computed. The study also addressed the problem of evaluating the error budget of the 2-D displacement time series obtained through the multi-track MinA technique. A comprehensive analysis, based on the knowledge of the statistical properties of the noise corrupting the computed differential SAR interferograms as well as the mathematical relationships existing among the different components of the ground deformation, has been performed. Of great concern is the study of the stability of the FPFC that was built to prevent the city from extreme flood events, which could be exacerbated in the future by the global climate changes and the associated sea level rise. In particular, our analysis has revealed that the SW part of the facility is more prone to deformation and that the lateral movements also affect the structure. Unfortunately, at the current stage, there is a lack of SAR data covering the whole area of interest over a long period, which prevents the generation of long-term deformation time series. Nonetheless, since the S-1A/B satellites are currently monitoring the city regularly, we expect to extend the investigations presented in this study to the whole area and perform further evaluations based on the new data.

Author statement

Qiang Wang: Methodology, **Qing Zhao**: Conceptualization, **Jingzhao Ding**: draft preparation, **Alexander A. Fedotov**: Investigation, Vladimir Badenko: Validation, **Min Liu**: Management, and **Antonio Pepe**: Supervision

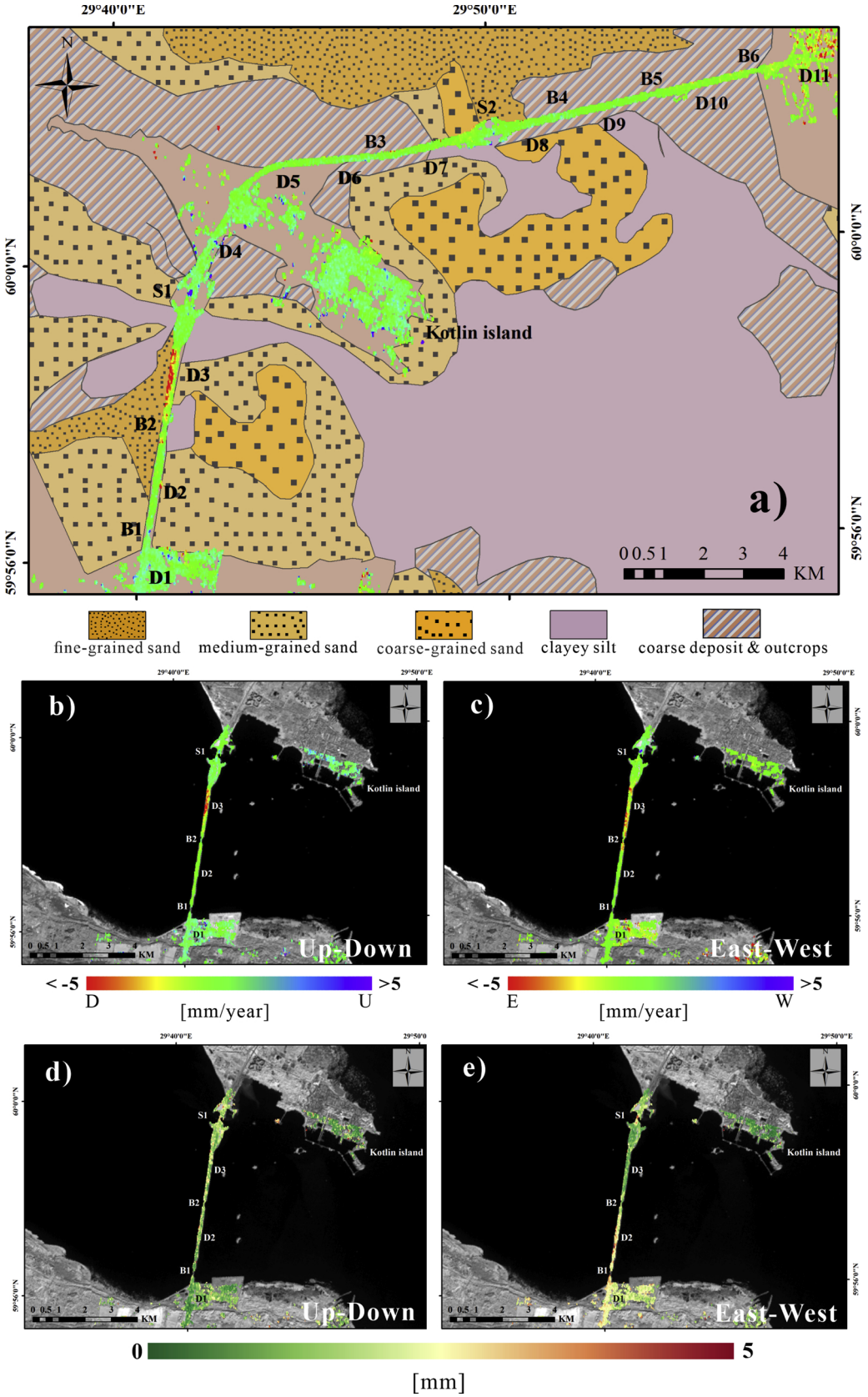

Fig. 12. a) LOS-projected mean deformation velocity map of the FPFC for 2016–2018; the base map is the lithologic map of the bottom surface of the Neva Bay and the eastern Gulf of Finland, partially referring to Philippov and Spiridonov (2009). Up-Down (b) and East-West (c) mean deformation velocity maps of the South-Western sector of the dam, and, RMSE maps for the Up-Down (d) and the East-West (e) ground deformation components are also presented.

Declaration of Competing Interest

The authors declare that they have no known competing financial interests or personal relationships that could have appeared to influence the work reported in this paper.

Acknowledgments

This work was supported by The National Key Research and Development Program of China [project no. 2017YFE0100700], by the Natural Science Foundation of China [# 41801337], by the Research Grant of Science and Technology Commission of Shanghai Municipality [project 18ZR1410800], by the Fundamental Research Funds for the Central Universities of China, by the Fund of the Director of the Key Laboratory of Geographic Information Science (Ministry of Education), East China Normal University [grant no. KLGIS2017C03], by the Ministry of Science and Higher Education of the Russian Federation within the framework of the Federal Program "Research and Development in Priority Areas for the Development of the Russian Science and Technology Complex for 2014-2020" [No. RFMEFI58417X0025]. This work was also performed within the Dragon 4 ESA project ID 32294. Sentinels and Landsat datasets were downloaded from the ESA Sentinel Hub and USGS Earth Explorer site, respectively. The authors would like to thank M. Rasulo, S. Guarino and F. Parisi, who have supported this work with their technical competences. We would also like to acknowledge the three anonymous reviewers for their helpful comments.

Appendix A. Supplementary data

Supplementary material related to this article can be found, in the online version, at doi:https://doi.org/10.1016/j.jag.2020.102050.

References

Aimaiti, Y., Yamazaki, F., Liu, W., 2018. Multi-sensor InSAR analysis of progressive land subsidence over the coastal city of Urayasu, Japan. Remote Sens. 10.
Badenko, V., Volgin, D., Lytkin, S., 2018. Deformation monitoring using laser scanned point clouds and BIM. MATEC Web of Conferences 245. pp. 01002.
Berardino, P., Fornaro, G., Lanari, R., Sansosti, E., 2002. A new algorithm for surface deformation monitoring based on small baseline differential SAR interferograms. IEEE Trans. Geosci. Remote. Sens. 40, 2375–2383.
Blewitt, G., Hammond, W.C., Kreemer, C., 2018. Harnessing the GPS data explosion for interdisciplinary science. Eos 99.
Colle, B.A., Buonaiuto, F., Bowman, M.J., Wilson, R.E., Flood, R., Hunter, R., Mintz, A., Hill, D., 2008. New York City's vulnerability to coastal flooding - Storm surge modeling of past cyclones. Bull. Am. Meteorol. Soc. 89, 829–841.
Costantini, M., 1998. A novel phase unwrapping method based on network programming. IEEE Trans. Geosci. Remote. Sens. 36, 813–821.
Dashko, R.E., Lebedeva, Y.A., 2017. Improving approaches to estimating hydrogeological investigations as a part of engineering survey in megacities: case study of St. Petersburg. Water Resour. 44, 875–885.
Draper, N.R., Smith, H., 1988. Applied Regression Analysis. Wiley, Hoboken, NJ, USA.
Fedorov, M., Badenko, V., Maslikov, V., Chusov, A., 2016. Site selection for flood detention basins with minimum environmental impact. Procedia Eng. 165, 1629–1636.
Ferretti, A., Prati, C., Rocca, F., 2001. Permanent scatterers in SAR interferometry. IEEE Trans. Geosci. Remote. Sens. 39, 8–20.
Franceschetti, G., Lanari, R., 1999. Synthetic Aperture Radar Processing. CRC Press, Boca Raton, FL, USA.
Filippova, Y., Matyushina, L., 2016. Main activities in the field of environment protection and environmental safety in operation of St. Petersburg metro facilities. Procedia Eng. 165, 461–468.
Gray, L., 2011. Using multiple RADARSAT InSAR pairs to estimate a full three-dimensional solution for glacial ice movement. Geophys. Res. Lett. 38.
Hooper, A., Zebker, H., Segall, P., Kampes, B., 2004. A new method for measuring deformation on volcanoes and other natural terrains using InSAR persistent scatterers. Geophys. Res. Lett. 31.
Ivanov, S.V., Kosukhin, S.S., Kaluzhnaya, A.V., Boukhanovsky, A.V., 2013. Simulation-based collaborative decision support for surge floods prevention in St. Petersburg (vol 3, pg 450, 2012). J. Comput. Sci. 4 438–438.
Kosterin, N.V., Shchekachikhin, V.I., 2017. St. Petersburg flood protection barrier system: first years of operation. Power Technol. Eng. 51, 371–376.
Kosukhin, S.S., Kalyuzhnaya, A.V., Nikishova, A.V., Boukhanovsky, A.V., 2015. Special aspects of wind wave simulations for surge flood forecasting and prevention. Procedia Comput. Sci. 66, 184–190.
Kozin, E., 2016. Safety operation assurance for metro artificial facilities during underground space development in St. Petersburg. Procedia Eng. 165, 418–432.
Massonnet, D., Feigl, K.L., 1998. Radar interferometry and its application to changes in the earth's surface. Rev. Geophys. 36, 441–500.
Milillo, P., Perissin, D., Salzer, J.T., Lundgren, P., Lacava, G., Milillo, G., Serio, C., 2016. Monitoring dam structural health from space: insights from novel InSAR techniques and multi-parametric modeling applied to the Pertusillo dam Basilicata, Italy. Int. J. Appl. Earth Observ. Geoinform. 52, 221–229.
Neokosmidis, S., Elias, P., Parcharidis, I., Briole, P., 2016. Deformation estimation of an earth dam and its relation with local earthquakes, by exploiting multitemporal synthetic aperture radar interferometry: Mornos dam case (Central Greece). J. Appl. Remote Sens. 10.
Novozhenin, S.U., Vystrchil, M.G., 2016. New method of surface settlement prediction for Sint-Petersburg metro escalator tunnels excavated by EPB TBM. Procedia Eng. 150, 2266–2271.
Pepe, A., Solaro, G., Calo, F., Dema, C., 2016. A minimum acceleration approach for the retrieval of multiplatform InSAR deformation time series. IEEE J. Sel. Top. Appl. Earth Obs. Remote. Sens. 9, 3883–3898.
Philippov, N.B., Spiridonov, M.A., 2009. Geological Atlas of St. Petersburg. http://www.infoeco.ru/geoinform/dl/atlas_eng.pdf.
Plant, G.W., Covil, C.S., Hughes, R.A., 1998. Geology, surveying, reclamation settlement. In: London, U.K. (Ed.), Site Preparation of the New Hong Kong International Airport, 1st ed. Thomas Telford 1998, pp. 45, 387–416, 515–517.
Shi, X.G., Zhang, L., Balz, T., Liao, M.S., 2015. Landslide deformation monitoring using point-like target offset tracking with multi-mode high-resolution TerraSAR-X data. ISPRS J. Photogramm. Remote. Sens. 105, 128–140.
Tofani, V., Raspini, F., Catani, F., Casagli, N., 2013. Persistent scatterer interferometry (PSI) technique for landslide characterization and monitoring. Remote Sens. 5, 1045–1065.
Tough, R.J.A., Blacknell, D., Quegan, S., 1995. A statistical description of polarimetric and interferometric synthetic aperture radar data. Proc. Math. Phys. Sci. 449 (1937), 567–589. https://doi.org/10.1098/rspa.1995.0059.
Ulitsky, V.M., Shashkin, A.G., Lisyuk, M.B., 2005. Analyses of historical buildings condition with respect to soil structure interaction. Proceedings of the Internatioanl Conference on Soil Mechnics and Geotechnical Engineering 16, 2769.
Wang, J., Gao, W., Xu, S.Y., Yu, L.Z., 2012. Evaluation of the combined risk of sea level rise, land subsidence, and storm surges on the coastal areas of Shanghai, China. Clim. Change 115, 537–558.
Wright, T.J., Parsons, B.E., Lu, Z., 2004. Toward mapping surface deformation in three dimensions using InSAR. Geophys. Res. Lett. 31.
Xu, B., Feng, G., Li, Z., Wang, Q., Wang, C., Xie, R., 2016. Coastal subsidence monitoring associated with land reclamation using the point target based SBAS-InSAR method: a case study of Shenzhen, China. Remote Sens. (Basel) 8.
Yin, J., Yu, D., Wilby, R., 2016. Modelling the impact of land subsidence on urban pluvial flooding: a case study of downtown Shanghai, China. Sci. Total Environ. 544, 744–753.
Zhao, Q., Pepe, A., Gao, W., Lu, Z., Bonano, M., He, M.L., Wang, J., Tang, X., 2015. A DInSAR investigation of the ground settlement time evolution of ocean-reclaimed lands in Shanghai. IEEE J. Sel. Top. Appl. Earth Obs. Remote. Sens. 8, 1763–1781.
Zhao, J., Wu, J., Ding, X., Wang, M., 2017. Elevation extraction and deformation monitoring by multitemporal InSAR of Lupu Bridge in Shanghai. Remote Sens. (Basel) 9.